Peer-reviewed version available at *Energies* **2018**, *11*, 814; doi:10.3390/en11040814

Article

Direct Flux Control for Stand-Alone Operation Brushless Doubly Fed Induction Generator Using Resonant-Based Sliding-Mode Control Approach

Kai Ji * and Shenghua Huang

State Key Laboratory of Advanced Electromagnetic Engineering and Technology, Huazhong University of Science and Technology, Address 1037 Luoyu Road, Wuhan 430074, China; jikai712@yeah.net
* Correspondence: jikai712@yeah.net; Tel.: +86-27-6889-6785/+86-13035135937

Abstract: In this paper, a novel voltage control strategy of stand-alone operation brushless doubly fed induction generator for variable speed constant frequency wind energy conversion systems was presented and discussed particularly. Based on the model of the generator power system, the proposed direct flux control strategy employs a nonlinear reduced-order generalized integrator based resonant sliding-mode control scheme to directly calculate and regulated the output value of converter which control winding stator required so as to eliminate the instantaneous errors of power winding stator flux, and no involving any synchronous rotating coordinate transformations. The stability, robustness and convergence capability of the proposed control strategy were described and analyzed. Owing to no extra current control loops involved, therefore simplifying the system configuration design and enhancing the transient performance. Constant converter switching frequency was achieved by using space vector pulse width modulation, which reduce the harmonic of generator terminal voltage. In addition, experimental results prove the feasibility and validity of the proposed scheme, and excellent steady and dynamic state performance is achieved.

Keywords: brushless doubly fed induction generator; direct control; stand-alone; sliding-mode; resonant; reduced-order generalized integrator; variable-speed constant-frequency; wind energy conversion systems

1. Introduction

Among variable-speed constant-frequency (VSCF) wind energy conversion systems (WECS), a brushless doubly-fed induction generator (BDFIG) as a low-cost but reliable option shares with the doubly-fed induction generator (DFIG)'s benefits of low cost construction in that no permanent magnets materials used and only a fractionally rated converter needed. Simultaneously, the absence of electric slip rings obviates one of the main failure modes of the DFIG [1–2]. The BDFIG also has a significantly improved low-voltage ride-through performance compared with DFIG [3]. Furthermore, it is a medium velocity generator, which increases the efficiency and the reliability because the high-speed gear stage is avoided.

The control of BDFIG systems have has received much more attention in research communities as well as industries than ever. In particular, classical power winding (PW) stator-flux-oriented (SFO) vector control (VC) presented in [4–8] decouples the control winding (CW) stator current into active and reactive power components in the PW stator synchronous reference frame. Control of instantaneous PW stator active and reactive powers is then achieved by regulating the decoupled CW currents, employing proportional-integral (PI) controllers. Moreover, VC-based unbalanced operation capability is investigated [6,7], the typical improved algorithm include employing two PI current regulators implemented in the positive and negative counter-rotating synchronous reference frame respectively [6], or using PI plus resonant (PIR) regulators to implement the precise control of

Peer-reviewed version available at Energies 2018, 11, 814; doi:10.3390/en11040814

both positive and negative-sequence currents in positive synchronous reference frame [7]. Besides, VC-based sensor-less control is developed as well [8]. The main drawback for VC is that the performance involving system stability and dynamic response highly relies on the tuning of the regulator parameters and accurate machine parameters. Thus, performance may degrade when actual machine parameters deviate from values used in the control system. Besides, additional outer control loop is required to generate the inter loop reference values. Considering discrete operation of voltage source converters (VSCs), direct control (DC), as an alternative to the VC, was proposed in [9–13]. Such strategy provides direct control of the machine's torque or power, reduces the complexity of the VC strategy and minimizes the use of machine parameters. Initially, the traditional lookup table (LUT) DC, as the name indicates, selects the proper voltage vectors directly from a predefined optimal switching signals table basis on the information of estimated machine's flux [9,10], and be further implemented in unbalanced situations [11]. Moreover, the synthetic vector direct torque control is proposed to solve the flux and torque losing control problems in [12]. Nevertheless, the main disadvantage is that the converter switching frequency varies with operating conditions and hysteresis controllers' bandwidth, As a result, the PW stator side filter preventing switching harmonics from injecting the connected grid needs to be designed to absorb broad-band harmonics spectrum, and the filter's efficiency is reduced with increased size and power losses. In addition, a high sampling frequency is used to guarantee acceptable steady and dynamic performances. To solve this issue highlighted, a model predictive DC strategy was presented in [13], the each voltage vector were chosen based on a basic switching table and thereafter their duration times were optimized with the cost function target of reduce ripple in the torque and flux. Although a constant switching frequency was achieved, it required complicated online calculations. Whereas another model-based predictive control strategy developed in [14], directly calculated required voltage vectors within each sampling period and used integrator to eliminate the errors, however, it was quite sensitive to system parameters' variations, moreover, implemented in the synchronous reference frame which necessitates the rotating coordinate transformations. Besides, an indirect stator-quantities control presented in [15], implemented in stationary reference frames avoids synchronous coordinate transformations, and torque and flux inner loops regulator incorporating pulse width modulation (PWM) was developed for provides the capability of current limit. Apparently, similar to VC, a simple linear approximation of the error can cause system performance degrade due to the nonlinear nature of VSC.

The investigation been primarily focused on grid-connected mode applications. On the other hand, for some local loads, only island grids are possible due to geographical or economic issues, in addition, the development of WECS has resulted in remote or island grids, and the distributed generation concept requires the generation system to be prepared to disconnect from the grid, in case of grid failure, and to maintain power supply to isolated loads. Consequently, the stand-alone generation system is becoming imperative. Meanwhile, not enough work has addressed the stand-alone operation mode relatively but a little literature developed in [14,16–19]. The SFO VC is designed and verified [16]. Furthermore VC-based inner loops decoupling network [17] is investigated, Moreover, PIR regulators implemented to elimination harmonic of nonlinear loads [18]. Nevertheless, VC scheme have the weak robustness to parameters' variations, etc. The predictive DC scheme [14] required complicated online calculations and so on. Whereas direct voltage control scheme [19] neglected the impact of load current to terminal voltage of PW stator. Moreover, the above methods were implemented in the synchronously rotating reference as well.

Variable structure control or sliding-mode control (SMC) strategy is an effective and high-frequency switching control for nonlinear systems with uncertainties. It features simple implementation, disturbance rejection, strong robustness, and fast responses, but the controlled state may exhibit undesired chattering. Thus, a SMC-based approach for DFIG driven by turbine has been proposed in [21–29]. In particular, a first-order SMC described in [22] put forward leads to a variable switching frequency of converter, this may course broadband harmonics. This drawback is overcome in [23] through application of the so-called boundary layer method. Nevertheless, the ultimate tracking accuracy and were partially lost. Furthermore, in order to maintain enhanced transient response and minimize steady-state error, the sliding-mode (SM) surfaces can be set as the integral forms [24]. Besides, for the sake of improve performance such as suppressing chattering-free behavior, several hybrid control techniques have been proposed such as higher order SMC [25,26] and adaptive SMC [27,28] , etc. The second-order SMC was proposed in [25] to regulate the *d*-and *q*-axis components with SFO, and to deal with either unbalanced or distorted grid voltage as well, however tuning the parameters of controllers is a challenging task. The fractional order SMC in [28,29] offers more degree of freedom due to its additional design parameters, hence be tuned for the optimum dynamic response, while the robustness remains, but it is not supported by sufficient experimental validation yet. Apparently, identical to VC scheme, all of the process still requires synchronous rotating coordinate transformation and angular information of stator flux. So far less literature associated with SMC for BDFIG.

In order to tackle the drawback highlighted earlier, this paper presents a novel direct flux control (DFC) scheme for stand-alone operation BDFIG using resonant(R)-based SMC approach. The proposed R-SM-DFC is capable of simply regulating the instantaneous PW stator flux without extra CW stator current control loops and synchronous rotating coordinate transformations involved. The required CW stator voltage can be directly obtained in PW stator stationary reference frame and a nonlinear reduced order generalized integrator (ROGI) based sliding surface is introduced. The space vector modulation (SVM) technique is employed afterward to achieve constant switching frequency. As a result, enhanced transient performance similar to the DC scheme is obtained and steady-state PW stator harmonic spectra are kept at the same level as the VC strategy. The rest part of the paper is organized as follows. In Section 2, with operation of BDFIG briefly summarized, the mathematical model and dynamic behavior is given. In Section 3, the ROGI based R-SM-DFC strategy is proposed, designed, and analyzed thoroughly. Section 4 presents the experimental results to demonstrate the performance of the strategy. Finally, the conclusions are made in Section 5.

2. BDFIG Stand-alone Operation and Model

2.1. Operation and configuration

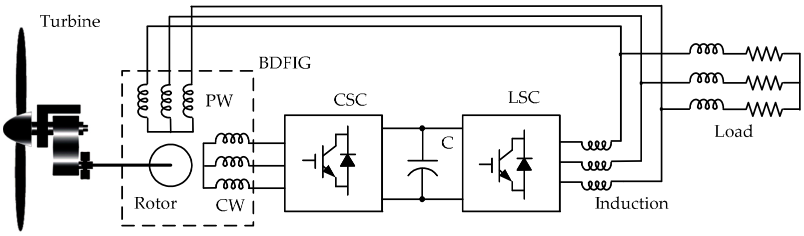

Figure 1. Topology of stand-alone BDFIG operation

The stator of the BDFIG is furnished with two separate stator windings, known as the PW and CW, which share one stator lamination and differ in pole pair numbers distribution to avoid direct coupling between the windings. The rotor employs a special design enabling it to couple to both stator windings [2]. Generally speaking, PW stator is connected to the point of common coupling (PCC) directly, whereas the CW stator is fed by a back-to-back VSC connected to the PCC, handling only a fraction of the rated power with limited velocity ranges. This topology shown in Figure 1 has the advantage of reducing the rating of the power electronics. The CW stator side converter (CSC) is designed to control the PW stator voltage terminal amplitude and frequency constant with variable-speed wind turbine. And the load side converter (LSC) keeps the direct-current (DC)-link voltage constant, meet the grid side harmonic acceptance indicator and guarantees the converter operation with an expected power factor. Quiet unlike the grid-connected mode application, a stand-alone power generation system itself has to generate a voltage and frequency in the PW stator terminal irrespective of varying rotational velocity due to wind turbine speeds and varying loads. Therefore, the PW stator terminal voltage’s amplitude and frequency stability is extremely mandatory to ensure overall satisfactory performance.

The BDFIG is normally operated in the synchronous mode, in which the shaft velocity is determined by the excitation frequencies of the two stator windings, independent of the torque exerted on the machine, the so-called synchronous rotor angular velocity can be expressed as:

$$\omega_r = \frac{\omega_p + \omega_c}{p_p + p_c} \tag{1}$$

Where ω_p and ω_c are the excitation angular frequencies supplied to PW (p_p pole pairs) stator and the CW (p_c pole pairs) stator respectively. Stator and rotor quantities are shown for the synchronous mode in Figure 2.

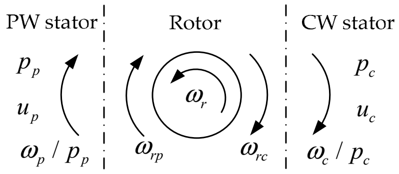

Figure 2. BDFIG synchronous mode of operation

2.2. Model and Dynamic Behavior of a BDFIG

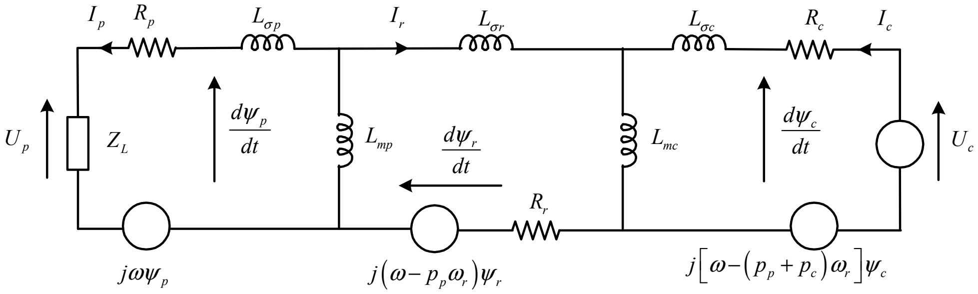

Figure 3. The dynamic equivalent circuit of a BDFIG in the arbitrarily reference frame

The equivalent circuit of a BDFIG represented in the unified reference frame with arbitrarily angular velocity rotating is shown in Figure 3, as it is shown, the generic dynamic vector model [30] in p_p-type pole pairs distribution can be expressed. The voltage vectors is given as:

$$\boldsymbol{U}_p^p = R_p \boldsymbol{I}_p^p + d\boldsymbol{\Psi}_p^p / dt + j\omega \boldsymbol{\Psi}_p^p \tag{2}$$

$$\boldsymbol{U}_c^p = R_c \boldsymbol{I}_c^p + d\boldsymbol{\Psi}_c^p / dt + j\left[\omega - \left(p_p + p_c\right)\omega_r\right]\boldsymbol{\Psi}_c^p \tag{3}$$

$$\boldsymbol{U}_r^p = R_r \boldsymbol{I}_r^p + d\boldsymbol{\Psi}_r^p / dt + j\left(\omega - p_p\omega_r\right)\boldsymbol{\Psi}_r^p \tag{4}$$

The flux linkage vectors is given as:

$$\boldsymbol{\Psi}_p^p = L_{sp}\boldsymbol{I}_p^p + L_{mp}\boldsymbol{I}_r^p \tag{5}$$

$$\boldsymbol{\Psi}_c^p = L_{sc}\boldsymbol{I}_c^p + L_{mc}\boldsymbol{I}_r^p \tag{6}$$

$$\boldsymbol{\Psi}_r^p = L_r\boldsymbol{I}_r^p + L_{mc}\boldsymbol{I}_c^p + L_{mp}\boldsymbol{I}_p^p \tag{7}$$

The electromagnetic torque equation is expressed:

$$T_e = \frac{3}{2} p_p \, Im\left[\boldsymbol{\Psi}_p^p \boldsymbol{I}_p^p\right] + \frac{3}{2} p_c \, Im\left[\boldsymbol{\Psi}_c^p \boldsymbol{I}_c^p\right] \tag{8}$$

Peer-reviewed version available at *Energies* **2018**, *11*, 814; doi:10.3390/en11040814

Where $\boldsymbol{U}$, $\boldsymbol{I}$, $\boldsymbol{\Psi}$, R, and L denote the voltage, current, flux linkage, resistance, and inductance parameters, respectively, T_e and ω is the electromagnetic torque of machine and rotational velocity, j represents the unit imaginary, Subscript m and s expresses the mutual and self inductance parameters, subscript r, p and c expresses the rotor, PW and CW stator parameters respectively, Superscript p expresses the PW stator reference frame, operator Im denote imaginary part of vector.

Considering the rotor voltage equation (4), $\boldsymbol{U}_r$=0, then rotor flux $\boldsymbol{\Psi}_r$ can be expressed as:

$$\boldsymbol{\Psi}_r^p = -\frac{R_r \boldsymbol{I}_r^p}{\left[d/dt + j(\omega - p_p \omega_r) \right]} \tag{9}$$

Noting that in a well designed BDFIG, the R_r has small values and negligible, meanwhile, the value of $d/dt + j(\omega - p_p \omega_r)$ is larger both in steady state and transient state. Evaluating the different factor values of equations (9), it can be concluded that $\boldsymbol{\Psi}_r$ is so smaller that can be assumed $\boldsymbol{\Psi}_r \approx 0$, then, according to rotor flux equations (7) the rotor current can be derived as:

$$\boldsymbol{I}_r^p = -\frac{L_{mc}}{L_r} \boldsymbol{I}_c^p - \frac{L_{mp}}{L_r} \boldsymbol{I}_p^p \tag{10}$$

Substituting equations (10) $\boldsymbol{I}_r$ to flux equations (5), (6), PW and CW stator flux linkage vectors can be can be simplified as follows:

$$\boldsymbol{\Psi}_p^p = A_p \boldsymbol{I}_p^p + A_m \boldsymbol{I}_c^p \tag{11}$$

$$\boldsymbol{\Psi}_c^p = A_c \boldsymbol{I}_c^p + A_m \boldsymbol{I}_p^p \tag{12}$$

Where $A_p = L_{sp} - L_{mp}^2 / L_r$, $A_c = L_{sc} - L_{mc}^2 / L_r$, and $A_m = -L_{mc} L_{mp} / L_r$. In the flux equations (11) and (12), the two stator electromagnetic coupling relationship is represented directly.

Based on PW stator flux equation (11), the CW stator current can be expressed as:

$$\boldsymbol{I}_c^p = \frac{\boldsymbol{\Psi}_p^p - A_p \boldsymbol{I}_p^p}{A_m} \tag{13}$$

Substituting equation (13) to CW stator flux equation (12) and systematizing it, then the instantaneous CW stator flux linkage can be expressed as:

$$\boldsymbol{\Psi}_c^p = \frac{A_c}{A_m} \boldsymbol{\Psi}_p^p - \frac{A_c A_p - A_m^2}{A_m} \boldsymbol{I}_p^p \tag{14}$$

Differentiating equation (14) results in instantaneous variations of CW stator flux as:

$$\frac{d\boldsymbol{\Psi}_c^p}{dt} = \frac{A_c}{A_m} \frac{d\boldsymbol{\Psi}_p^p}{dt} - \frac{A_c A_p - A_m^2}{A_m} \frac{d\boldsymbol{I}_p^p}{dt} \tag{15}$$

Substituting equation (14) and (15) to CW stator voltages equation (6), and systematizing it, then, the instantaneous variations of PW stator flux can be derived as:

$$\frac{d\boldsymbol{\Psi}_p^p}{dt} = \frac{A_m}{A_c} \boldsymbol{U}_c^p - \left\{ \frac{A_m}{A_c} R_c + jA_m \left[\omega - \left(p_p + p_c \right) \omega_r \right] \right\} \boldsymbol{I}_c^p - j\frac{A_m^2}{A_c} \left[\omega - \left(p_p + p_c \right) \omega_r \right] \boldsymbol{I}_p^p + \frac{A_c A_p - A_m^2}{A_c} \frac{d\boldsymbol{I}_p^p}{dt} \tag{16}$$

It is worthy noting that, the model and dynamic behavior can be represented in the PW synchronous rotating *d-q* reference frame by setting $\omega = \omega_p$, or in PW stationary α-β reference frame by setting ω=0 in equations (2)-(16).

3. Proposed DFC Using R-SMC Approach

3.1. Reference flux quantity

The stand-alone operation BDFIG must supply constant voltage and frequency at the PW stator terminals irrespective of the varying shaft rotational velocity due to wind turbine speeds and varying loads. PW stator voltage is indirectly determined through PW stator flux which is regulated by CW stator excitation current, thus the reference quantity can be set as PW stator flux. PW stator voltage phase angle can be derived directly from a free running integral of the PW stator frequency reference, and according to PW stator voltage equation (2), the commanded PW stator flux value is calculated from integration of the PW stator back electromotive force (EMF) references:

$$\boldsymbol{\Psi}^{p}_{p\alpha\beta} = \int \left(\boldsymbol{U}^{p}_{p\alpha\beta} - R_p \boldsymbol{I}^{p}_{p\alpha\beta} \right) dt \tag{17}$$

As the flux estimation proposed in equations (17) will produce direct-current (DC) drift at low frequency in this implementation. The DC drift is extracted and eliminated with a low-pass filter instead of pure integrator. In addition, generally speaking, the integral model is irrelevant to the more generator parameters, except for the PW stator resistance whose impact on the system performance is negligible because of the resistance voltage drop is smaller relatively high grid frequency.

3.2. Sliding Surface

The control objectives for stand-alone operation BDFIG systems are to track or slide along the predefined PW stator flux trajectories. Thus the sliding switching surface is set as:

$$\boldsymbol{S} = \begin{bmatrix} S_1 & S_2 \end{bmatrix}^T \tag{18}$$

The derivation of resonant sliding surface is based on the stationary reference frame implementation of a synchronous integrator. In the PW synchronous rotating reference frame, both the current references and disturbance is characterized by a DC signals in steady state, In order to maintain the enhanced transient response and minimize the steady-state error, the sliding switching surfaces can be set as the integral form generally [23,24].

$$\boldsymbol{S}_{dq} = \left(1 + \boldsymbol{K}/s\right) \boldsymbol{E}^{p}_{\Psi dq} \tag{19}$$

Where, $\boldsymbol{E}^{p}_{pdq} = \boldsymbol{\Psi}^{p*}_{pdq} - \boldsymbol{\Psi}^{p}_{pdq}$ is the instantaneous error between the references and the actual values, $\boldsymbol{K}$ is positive control gain coefficient matrix, and s is the derivative operator. An integrator implemented in synchronous reference frame with input $\boldsymbol{X}_{dq}$ and output $\boldsymbol{Y}_{dq}$ is described by:

$$s\boldsymbol{Y}_{dq} = \boldsymbol{X}_{dq} \tag{20}$$

Nevertheless, integral sliding surfaces can only regulate the DC signals of the feedbacks to track the references in the synchronous reference frame but not alternating-current (AC) signals in stationary reference frame due to the lower amplitude responses at high frequency. Note that the relation between the variables in the synchronous rotating frame and the stationary frame is $\boldsymbol{X}_{dq} = e^{-j\theta} \boldsymbol{X}_{\alpha\beta}$, thus the integrator may be transformed to stationary reference frame by taking a frequency shift of $-\omega$ for the positive sequence, the stationary frame generalized integrator(SGI) is mostly performed from equivalent synchronous rotating frame integrator whose transfer function be given as:

$$G_{ROGI}(s) = \frac{K}{s - j\omega} \tag{21}$$

SGI herein also named ROGI relative to second-order generalized integrator (SOGI), it must be noted that with two ROGI a SOGI can be constructed:

$$G_{SOGI}\left(s\right)=\frac{2sK}{s^2+\omega^2}=\frac{K}{s-j\omega}+\frac{K}{s+j\omega} \tag{22}$$

The fewer states in the ROGI's implementation against the SOGI's and the close relation between both are the reasons why is named ROGI. Therefore, the ROGI requires less computational burden [31]. In addition, both SOGI and ROGI are resonant controller that eliminate the sinusoidal tracking error thanks to its infinite gain and zero phase shift to special orders resonant frequency signals, but ROGI can provide discrimination between positive and negative sequence signals. ROGI's open-loop transfer function frequency response (magnitude and phase) be shown in Figure 4a. In fact, utilization of resonant controllers in AC tracking systems is a straight forward outcome of internal model principle [31], stating that in case to achieve zero steady-state error in a stable feedback system, the loop gain must contain a model, which can generate the required reference and disturbance signals, calling for integrative controller in DC systems and resonant controller in AC systems. In the stationary frame, both the reference and disturbance behaves AC signal. Therefore, there should be a sinusoidal internal model in the controller so as to eliminate the tracking error in special orders. Besides, the magnitude and phase response changes precipitously at the adjacent of resonant frequency, therefore the steady state control accuracy and stability would be deteriorated due to frequency deviates. In order to reduce the sensitivity toward slight frequency variations and increase the bandwidth around the resonant frequency, a component with cutoff frequency ω_c is inserted to provide a well compromise in practice. As seen from the Bode diagram of improved quasi ROGI's open-loop transfer function with different bandwidth coefficients in Figure 4b, response at the adjacent of resonant frequency show a much smoother changing, thus the better robustness of steady state accuracy against frequency deviation can be guaranteed.

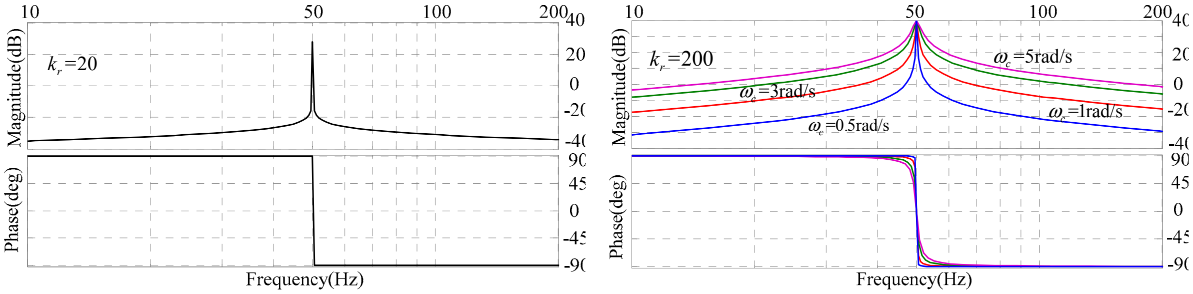

(**a**) (**b**)

Figure 4. Open-loop transfer function frequency response (magnitude and phase): (**a**) ROGI; (**b**) improved quasi ROGI with different bandwidth coefficients.

Then, an improved ROGI resonant sliding surface which be tuned at fundamental frequency is defined as equation (23) for PW stator stationary reference frame.

$$\boldsymbol{S}_{\alpha\beta}=\left(1+\frac{K\omega_{cp}}{s-j\omega_p+\omega_{cp}}\right)\boldsymbol{E}^{p}_{\Psi\alpha\beta} \tag{23}$$

3.3. SMC Law

In an SMC design, as the name indicates, the task is to force the system state trajectory to the interaction of the switching surfaces mentioned earlier. In this section, an SMC scheme is designed to generate the converter output voltage reference.

The manifold $\boldsymbol{S}$=0 represent the precise tracking of PW stator flux. When the system states reach the sliding manifold and slide along the surface, then we have:

$$\boldsymbol{S}_{\alpha\beta}=d\boldsymbol{S}_{\alpha\beta}/dt=0 \tag{24}$$

According to equation (23) and (24), derivatives of $\boldsymbol{S}$ equal zero, which gives:

Peer-reviewed version available at Energies 2018, 11, 814; doi:10.3390/en11040814

$$d\boldsymbol{E}_{\Psi\alpha\beta}^{p} \big/ dt = -\boldsymbol{K}\boldsymbol{E}_{\Psi\alpha\beta}^{p} \tag{25}$$

The aforementioned equations ensure the PW stator flux errors converge to zero, positive control gain matrix ***K*** is chosen for the required system transients. PW stator flux will converge asymptotically to the reference value with time constant matrix of 1/***K***. Then, the design task is aimed at accomplishing sliding mode in the manifolds ***S***=0 with discontinuous CW stator voltage space vectors.

$$\frac{d\boldsymbol{S}_{\alpha\beta}}{dt} = \frac{d\boldsymbol{E}_{\Psi\alpha\beta}^{p}}{dt} + \boldsymbol{K}\boldsymbol{E}_{\Psi\alpha\beta}^{p} = -\frac{d\boldsymbol{\Psi}_{p\alpha\beta}^{p}}{dt} + \boldsymbol{K}\left(\boldsymbol{\Psi}_{p\alpha\beta}^{p*} - \boldsymbol{\Psi}_{p\alpha\beta}^{p}\right) \tag{26}$$

Setting ω=0 in equation (16) for stationary reference frame and substituting it into equation (26), then leads to:

$$d\boldsymbol{S}_{\alpha\beta} \big/ dt = \boldsymbol{F} + \boldsymbol{B}\boldsymbol{U}_{c\alpha\beta}^{p} \tag{27}$$

Where,

$$\boldsymbol{B} = A_m \big/ A_c \text{ , } \boldsymbol{U}_{c\alpha\beta}^{p} = \begin{bmatrix} u_{c\alpha} & u_{c\beta} \end{bmatrix}^{T}$$

And,

$$\boldsymbol{F} = \left[\frac{A_m}{A_c} R_c - jA_m\left(p_p + p_c\right)\omega_r\right]\boldsymbol{I}_{c\alpha\beta}^{p} - j\frac{A_m^2}{A_c}\left(p_p + p_c\right)\omega_r \boldsymbol{I}_{p\alpha\beta}^{p} - \frac{A_c A_p - A_m^2}{A_c}\frac{d\boldsymbol{I}_{p\alpha\beta}^{p}}{dt} + \boldsymbol{K}\left(\boldsymbol{\Psi}_{p\alpha\beta}^{p*} - \boldsymbol{\Psi}_{p\alpha\beta}^{p}\right)$$

Splitting ***F*** into α-β components and arranging them in matrix form yield:

$$\boldsymbol{F} = \begin{bmatrix} F_1 & F_2 \end{bmatrix}^{T}$$

$$\begin{bmatrix} F_1 \\ F_2 \end{bmatrix} = \begin{bmatrix} \frac{A_m}{A_c} R_c & A_m\left(p_p + p_c\right)\omega_r \\ -A_m\left(p_p + p_c\right)\omega_r & \frac{A_m}{A_c} R_c \end{bmatrix}\begin{bmatrix} i_{c\alpha} \\ i_{c\beta} \end{bmatrix} + \begin{bmatrix} & \frac{A_m^2}{A_c}\left(p_p + p_c\right)\omega_r \\ -\frac{A_m^2}{A_c}\left(p_p + p_c\right)\omega_r & \end{bmatrix}\begin{bmatrix} i_{p\alpha} \\ i_{p\beta} \end{bmatrix}$$
$$- \begin{bmatrix} \frac{A_c A_p - A_m^2}{A_c} & \\ & \frac{A_c A_p - A_m^2}{A_c} \end{bmatrix}\frac{d}{dt}\begin{bmatrix} i_{p\alpha} \\ i_{p\beta} \end{bmatrix} + \begin{bmatrix} K_\alpha\left(\psi_{p\alpha}^{*} - \psi_{p\alpha}\right) \\ K_\beta\left(\psi_{p\beta}^{*} - \psi_{p\alpha}\right) \end{bmatrix}$$

In SMC, a Lyapunov approach is used for deriving conditions on the control law that will drive the state orbit to the equilibrium manifold. The quadratic Lyapunov function is selected as:

$$W = \boldsymbol{S}^{T}\boldsymbol{S} \big/ 2 \geq 0 \tag{28}$$

The time derivative of W on the state trajectories of equation (28) is given by:

$$\frac{dW}{dt} = \frac{1}{2}\left(\boldsymbol{S}^{T}\frac{d\boldsymbol{S}}{dt} + \boldsymbol{S}\frac{d\boldsymbol{S}^{T}}{dt}\right) = \boldsymbol{S}^{T}\frac{d\boldsymbol{S}}{dt} = \boldsymbol{S}^{T}\left(\boldsymbol{F} + \boldsymbol{B}\boldsymbol{U}_{c\alpha\beta}^{p}\right) \tag{29}$$

The switch control law must be chosen so that the time derivative of W is definitely negative with ***S***≠0. Thus, the following control law is selected:

$$\boldsymbol{U}_{c\alpha\beta}^{p} = -\boldsymbol{B}^{-1}\left\{\begin{bmatrix} F_1 \\ F_2 \end{bmatrix} + \begin{bmatrix} K_\alpha & 0 \\ 0 & K_\beta \end{bmatrix}\begin{bmatrix} sgn\left(S_1\right) \\ sgn\left(S_2\right) \end{bmatrix}\right\} \tag{30}$$

Where $sgn(S_1)$ and $sgn(S_2)$ are respective switch functions for α-β components flux of PW stator. From equation (30), the control law can be divided into two parts: the linear equivalent control part and the nonlinear switching control part. The equivalent control is used to control the nominal plant model, and the switching control is added to ensure the desired performance despite parametric uncertainty.

3.4. Proof of the Stability

For stability to the sliding surfaces, it is sufficient to have $dW/dt<0$. By setting appropriate switch functions, the stability can be achieved provided the following condition is satisfied:

If $S_1 sgn(S_1) > 0$ and $S_2 sgn(S_2) > 0$ then:

$$\frac{dW}{dt} = \boldsymbol{S}^T \frac{d\boldsymbol{S}}{dt} = -\boldsymbol{S}^T \begin{bmatrix} K_\alpha & 0 \\ 0 & K_\beta \end{bmatrix} \begin{bmatrix} sgn(S_1) \\ sgn(S_2) \end{bmatrix} \tag{31}$$

The time derivative of Lyapunov function dW/dt is definitely negative so that the control system becomes asymptotically stable.

3.5. Proof of the Robustness

In the practical operation, the sliding surface $\boldsymbol{S}$ will be affected by the parameter variations, AD sample errors, measurement noises, and so on. Thus, equation (27) should be rearranged as:

$$d\boldsymbol{S}/dt = \boldsymbol{F} + \boldsymbol{B}\boldsymbol{U}_{c\alpha\beta}^{p} + \boldsymbol{H} \tag{32}$$

Where $\boldsymbol{H} = \begin{bmatrix} H_1 & H_2 \end{bmatrix}^T$ represent system disturbances.

Thus, equation (30) can be rewritten as:

$$\frac{dW}{dt} = \boldsymbol{S}^T \frac{d\boldsymbol{S}}{dt} = \boldsymbol{S}^T \left\{ \begin{bmatrix} H_1 \\ H_2 \end{bmatrix} - \begin{bmatrix} K_\alpha & 0 \\ 0 & K_\beta \end{bmatrix} \begin{bmatrix} sgn(S_1) \\ sgn(S_2) \end{bmatrix} \right\} \tag{33}$$

It is worth noting that if the positive control gains fulfill the following condition, namely, $K_\alpha > |H_1|$ and $K_\alpha > |H_1|$, the time derivative of Lyapunov function dW/dt is still definitely negative. Thus, the SMC features strong robustness.

3.6. Remedy of Chattering Problem

The SMC scheme developed earlier guarantees the fast tracking of the instantaneous components. However, fast switching may generate unexpected chattering, which may excite unmodeled high-frequency system transients and even result in unforeseen instability. To eliminate this problem, the discontinuous part of the controller is smoothed out by introducing a boundary layer around the sliding surface. As a result, a continuous function around the sliding surface neighborhood is obtained as:

$$sgn(S_j) = \begin{cases} 1, & \text{if } S_j > \lambda_j \\ S_j/\lambda_j, & \text{if } |S_j| \le \lambda_j \\ -1, & \text{if } S_j < -\lambda_j \end{cases} \tag{34}$$

Where $\lambda_j > 0$ is the width of the boundary layer and $j = 1, 2$.

3.7. Stationary Reference Frame Coordinate Transformations

In this control scheme, CW stator voltage and current magnitudes are expressed in a PW stator stationary reference frame. To express a magnitude $\boldsymbol{Z}$ from the CW stator (p_c-type pole pairs) stationary α-β reference frame transform into PW stator (p_p-type pole pairs) stationary α-β reference frame, the following relation can be used.

$$\mathbf{Z}^{c}_{c\alpha\beta} = \mathbf{Z}^{p}_{c\alpha\beta} e^{-j\left(p_p + p_c\right)\left(\theta_r + \delta\right) + p_c \gamma} \tag{35}$$

Where, superscript *p*, *c* expresses the PW stator and CW stator reference frame, respectively. The spatial relationship of CW stator and PW stator stationary α-β reference frames is shown in Figure 5a, it should be noticed that rotor position angular θ_r measurement is needed to transform a CW stator to a PW stator stationary α-β reference frame. The initial rotor position δ is needed to obtain correct alignment. The coefficient γ is the mechanical angular displacement between the two windings of the stator. The different reference axis and initial mechanical angular is shown in Figure 5b.

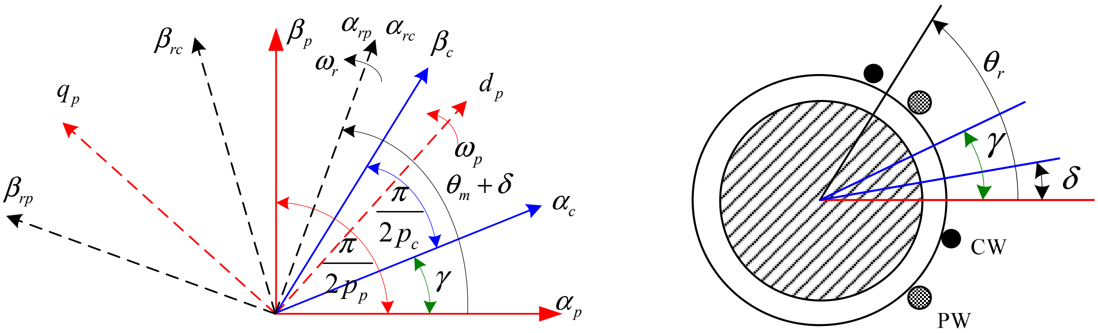

(**a**) (**b**)

Figure 5. The CW and PW stator stationary α-β reference frames. (**a**) The spatial relationship of CW and PW stator stationary α-β reference frames; (**b**) The different reference axis and initial mechanical angular.

3.8 CW Stator-side Output Voltage Limit

For a BDFIG, the maximum output voltage from the CSC is usually within the range of 30% of the PW stator voltage. Under steady-state operation, the required CW stator voltage is unlikely to exceed the output voltage limit of the CSC. However, during transient conditions, large and abrupt power variations of load can result in large PW voltage errors within one sampling period. Consequently, the CW stator voltage calculated using equation (30) and (35) may exceed the maximum output voltage capability of the CSC denoted as $\boldsymbol{U}_{cmax}$. Practically, in engineering implementations, the limiter is also needed to avoid large stress on mechanical or electrical components. Therefore, CW stator voltage must be scaled proportionally to improve the transient response. This process can be represented as:

$$\begin{cases} u^{*}_{c\alpha}{}' = \dfrac{u^{*}_{c\alpha}}{\sqrt{u^{*\,2}_{c\alpha} + u^{*\,2}_{c\beta}}} U_{c\,max} \\ u^{*}_{c\beta}{}' = \dfrac{u^{*}_{c\beta}}{\sqrt{u^{*\,2}_{c\alpha} + u^{*\,2}_{c\beta}}} U_{c\,max} \end{cases} \tag{36}$$

CW stator voltage limit could result in PW stator voltage magnitude being temporarily sag, in this case, the LSC serve as a static volt-ampere reactive generator by injecting a compensate current at the PCC to support voltage [20].

3.9 Voltage Vector Calculation Using SVM

The SVM is employed to generate the required switching voltage vectors and their respective duration times based on the required average CW stator voltage vector calculated in equation (36). For a three phase two-level VSC feeding CW stator, which the simplified configuration be shown in

Peer-reviewed version available at *Energies* **2018**, *11*, 814; doi:10.3390/en11040814

Figure 6, the output voltages can be represented by a voltage vector, and according to the levels of each phase, there are six active voltage vectors with amplitudes of $2U_{dc}/3$ and two zero voltage vectors. Figure 7a shows these eight fundamental voltage vectors denoted as $\boldsymbol{U}_0$–$\boldsymbol{U}_7$, where the subscript of $\boldsymbol{U}$ is derived from the binary number expressing the switching pattern in the phase sequence (a, b, c).

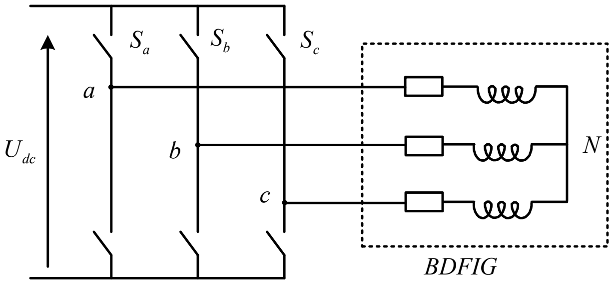

Figure 6. Simplified configuration of three phase two-level VSC

For the example shown in Figure 5a, where the average CW stator voltage vector $\boldsymbol{U}_c$ is located between $\boldsymbol{U}_6$ and $\boldsymbol{U}_2$, the voltage vectors required to resemble $\boldsymbol{U}_c$ are $\boldsymbol{U}_7$,$\boldsymbol{U}_6$,$\boldsymbol{U}_2$, and $\boldsymbol{U}_0$, and their respective durations are calculated as equation (37). CW stator voltage vectors and the impact of CW voltage vectors on the CW stator current be shown in Figure 7b.

$$t_a = \sqrt{3}k_v T_s \sin\left(\frac{\pi}{3}-\theta\right), \quad t_b = \sqrt{3}k_v T_s \sin(\theta), \quad t_{01} = t_{01} = \frac{T_s}{2}\left[1-\sqrt{3}k_v \sin\left(\frac{\pi}{3}+\theta\right)\right] \tag{37}$$

Where $k_v = \left|\boldsymbol{U}_c\right|/U_{dc}$, and $0 \le \theta \le \pi/3$.

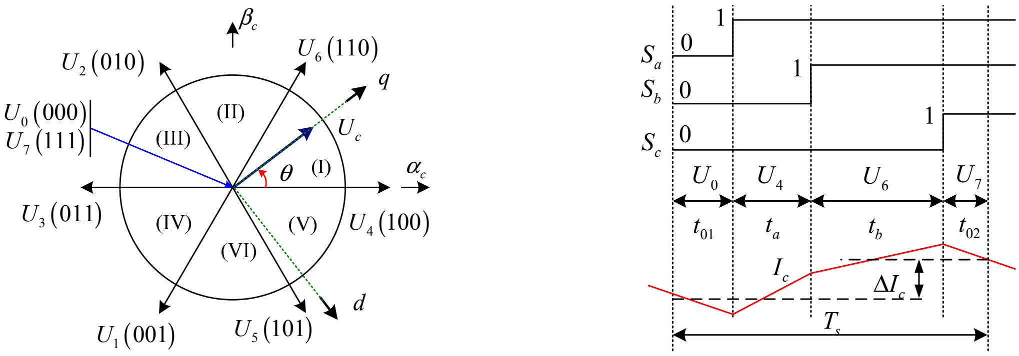

(**a**) (**b**)

Figure 7. Voltage vector calculation using SVM. (**a**) CW stator voltage vectors in the CW stator stationary reference frames; (**b**) CW stator voltage vectors and their impact on the CW stator current.

In the case of over-modulation, the zero voltage vector durations t_{01} and t_{02} calculated using equation (37) can become negative. Thus, the t_a and t_b must be scaled as:

$$t_a' = \frac{t_a}{t_a+t_b}T_s, \quad t_b' = \frac{t_b}{t_a+t_b}T_s, \quad t_{01} = t_{01} = 0 \tag{38}$$

The SVM is differ from LUT hysteresis modulation which results in deterministic narrowband harmonic spectra with dominant harmonics around the fixed switching carrier frequency and multiples thereof.

3.10 Control System Implementation

Based on the developed control strategies, the overall schematic diagram of proposed DFC strategy for a stand-alone operation BDFIG system employing the ROGI based R-SMC approach is

Peer-reviewed version available at Energies 2018, 11, 814; doi:10.3390/en11040814

shown in Figure 8. As can be seen and previously described, Both PW stator voltage, current and CW stator currents is sampled and transformed to the PW stator stationary reference respectively. The reference of the phase angle is derived directly from a free running integral of the PW stator frequency reference. The rotor position angle θ_r can be measured by the encoder. The PW stator flux value can be directly estimated according to integration of the PW stator back EMF which is irrelevant to the more generator parameters, except for the stator resistance. The instantaneous error of PW stator flux can be calculated by comparing the feedback quantity and reference quantity. The control law developed in equation (30) based on the ROGI resonant sliding surface as equation (23) are employed, and it simply regulate the instantaneous error of PW stator flux and directly generates the CW stator voltage reference for the CSC without any extra CW stator current control inter loops so as to enhanced transient performance. Afterward, it is transformed into CW stator stationary reference. Moreover, the reference of the CW stator voltage is limited properly to improve the transient response. In addition, SVM technique is employed to generate the switching patterns and their respective duration times, besides, achieve constant switching frequency which results in deterministic narrowband harmonic spectra with dominant harmonics around the carrier frequency and multiples thereof in CW stator voltage. Finally, it is worth noting that the proposed control scheme is implemented in the PW stator stationary reference frame hence no extra synchronous rotating coordinate transformations and angular information of grid voltage or PW stator flux involved.

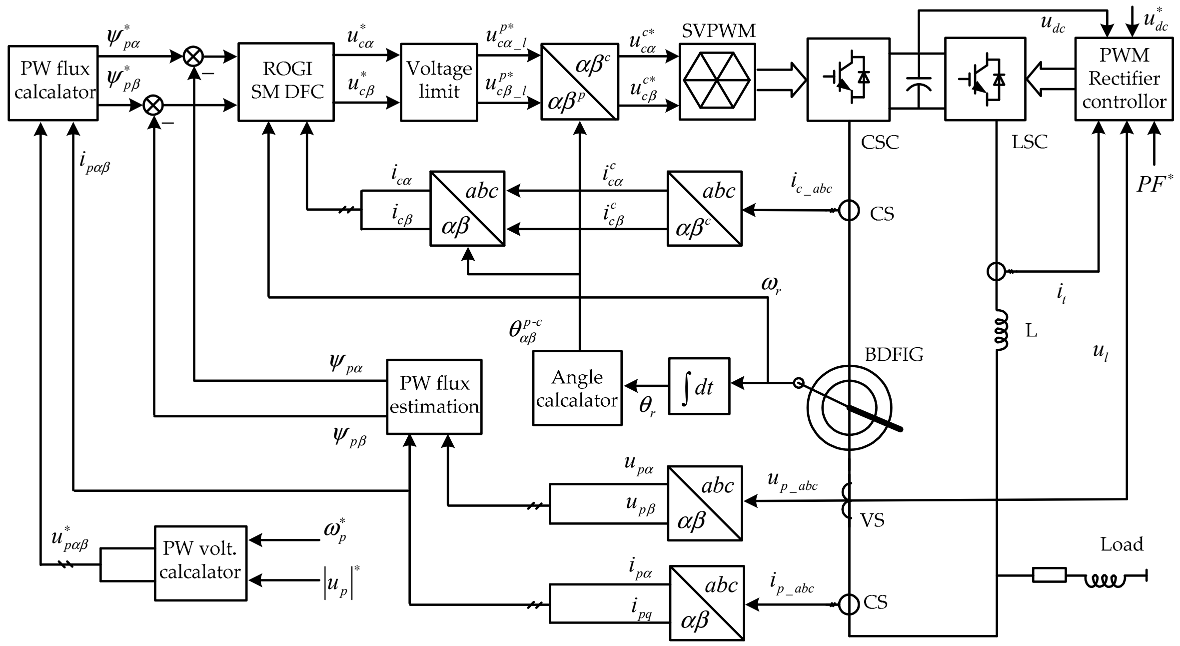

Figure 8. Schematic diagram of the proposed R-SM-DFC for a stand-alone operation BDFIG.

4. Experimental and Discussion Section

4.1. Test Rig Setup

In order to verify the steady and dynamic state performance and effectiveness of the proposed control strategy, the experimental tests were carried out on the small scaled test rig of reduced capacity prototype BDFIG whose parameters is shown in Table I respectively. The experimental test rig system is shown in Figure 9. In this test rig, as can be seen, a DC machine equipped with a commercial thyristor drive converter (DCS800 from ABB) is mechanically coupled to the BDFIG shaft emulated as a wind turbine with the speed control. An encoder of 2048 pulses per revolution is mounted on the shaft to detect the rotor position angular. The voltages and currents of each stator winding are sampled by LEM sensor, respectively. The CSC and LSC are fed by an insulated gate bipolar transistor (IGBT) based PWM VSC in which control strategy is implemented on the Texas

Instruments(TI)' 32 bit floating digital signal processor (DSP) TMS320F28335. The AD sampling and switching frequencies are 2kHz and 1kHz, respectively. The high-frequency switching in the VSC will give rise to sideband harmonic groups, whose frequencies are around carrier frequency and its multiples, due to the cross-coupling effect between the PW stator and CW stator, the CW stator voltage harmonic components will induce a mass of harmonics in the PW stator voltage. Therefore, a LC filter be installed in CW stator terminal to extracts the sinusoidal fundamental component of PWM voltage. The PW stator is connected to a three-phase switched resistive bank and a squirrel cage induction machine to supply a resistance and inductance load. The control parameters are tuned through experiments. The voltage and current are measured by Tektronix's probes, and all the waveforms are acquired by a YOKOGAWA DL750 digital storage oscilloscope. The experimental data can be imported into Matlab which implement discrete fast Fourier transform (FFT) to harmonic spectrum analysis.

Table 1. Prototype BDFIG parameters.

Parameter	Value	Parameter	Value	Parameter	Value
frame size	D250	rotor type	wound rotor	R_p	2.73 ohm
PW pole-pairs	1	CW pole-pairs	3	R_c	1.16ohm
PW connection	star	CW connection	star	R_r	0.1822ohm
PW rated volt.	380V	CW volt.	0-350V	L_p	0.4519H
PW rated freq.	50Hz	CW freq. range	-10-30Hz	L_c	0.4977H
PW rated current	45A	CW current range	0-40A	L_r	0.0366H
capacity	30kVA	efficiency	78-85%	L_{mp}	0.1175H
weight	385kg	volume	$0.27m^3$	L_{mc}	0.3359H

The experimental tests were performed as follows. The reference amplitude and frequency of the PW stator terminal outer voltage is set at 220 V and 50 Hz respectively in both case.

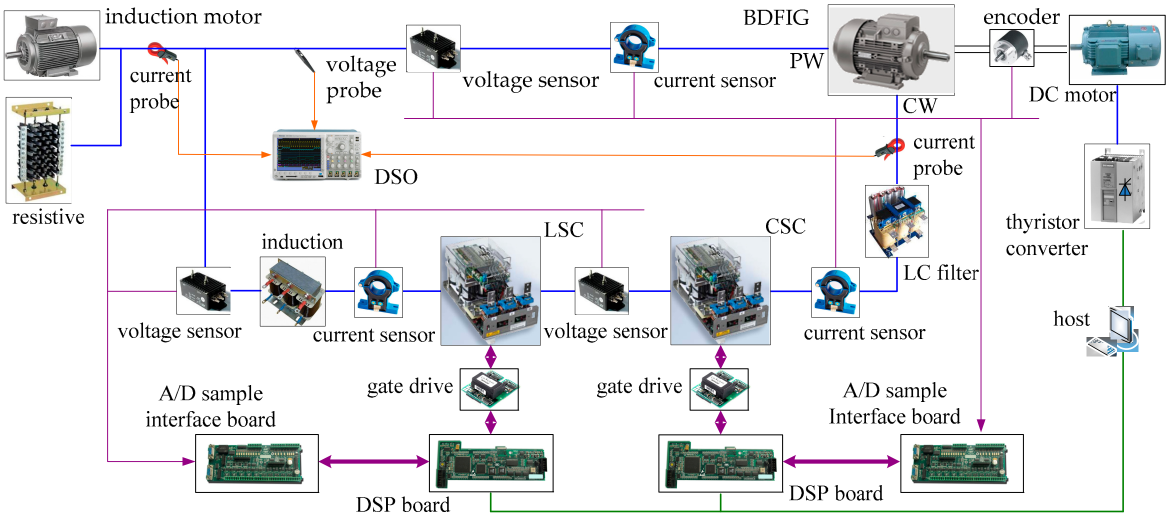

Figure 9. Schematic diagram of the experimental test rig system

4.2. Steady State Performance of Stand-alone operation BDFIG

The R-SM-DFC's steady state performance of stand-alone operation BDFIG fed with a constant linear resistance and inductance loads of 1.2kVA is presented at a fixed wind speed as shown in Figure 10a–j. Figure 10a–d shows the steady state recorded waveforms of PW stator terminal line voltage, load line current, CW stator phase current, rotor rotational velocity and its time's partial enlarged detail in sub-synchronous rotor rotational velocity of 0.867p.u.(650 rpm) and 0.933 p.u.(700 rpm), respectively. Obviously, both the amplitude and frequency of the PW stator terminal voltage are constant and accurately consistent with reference value, and sinusoidal PW stator voltage was generated with low harmonic distortion. The CW stator frequency is equal to 6.66 Hz and 3.33 Hz respectively, and met the relationship of equation (1) to maintain constant PW stator frequency. FFT analysis of PW stator terminal voltage is done, as shown in Figure 10i, the total harmonics distortion (THD) of PW terminal stator voltage is found to be 0.95% in 0.933p.u.(700rpm) velocity, which are maintained under the acceptable limits of an IEEE-519 Standard. It is due to stable control performance, besides, BDFIG have higher equivalent leakage impedance relatively DFIG which also has certain filtering effect. In this case, load power is less than the PW stator generated power in practice, so, the remaining power is feeding to the CW stator through the LSC. The BDFIG's steady state operation performance in super-synchronous rotor rotational velocity of 1.067p.u.(800rpm) and 1.133p.u.(850rpm) are also demonstrated in Figure 10e–h, respectively, the amplitude and frequency of the PW stator terminal voltage are stable, the THD is 0.86% in 1.067p.u.(800rpm) velocity as shown in Figure 10j. Just unlike the case of sub-synchronous velocity, load power is more than the PW stator terminal generated power and is about the sum of PW stator terminal generated power and CW stator power through LSC as well. In both cases, the generator proves good steady-state power output performance.

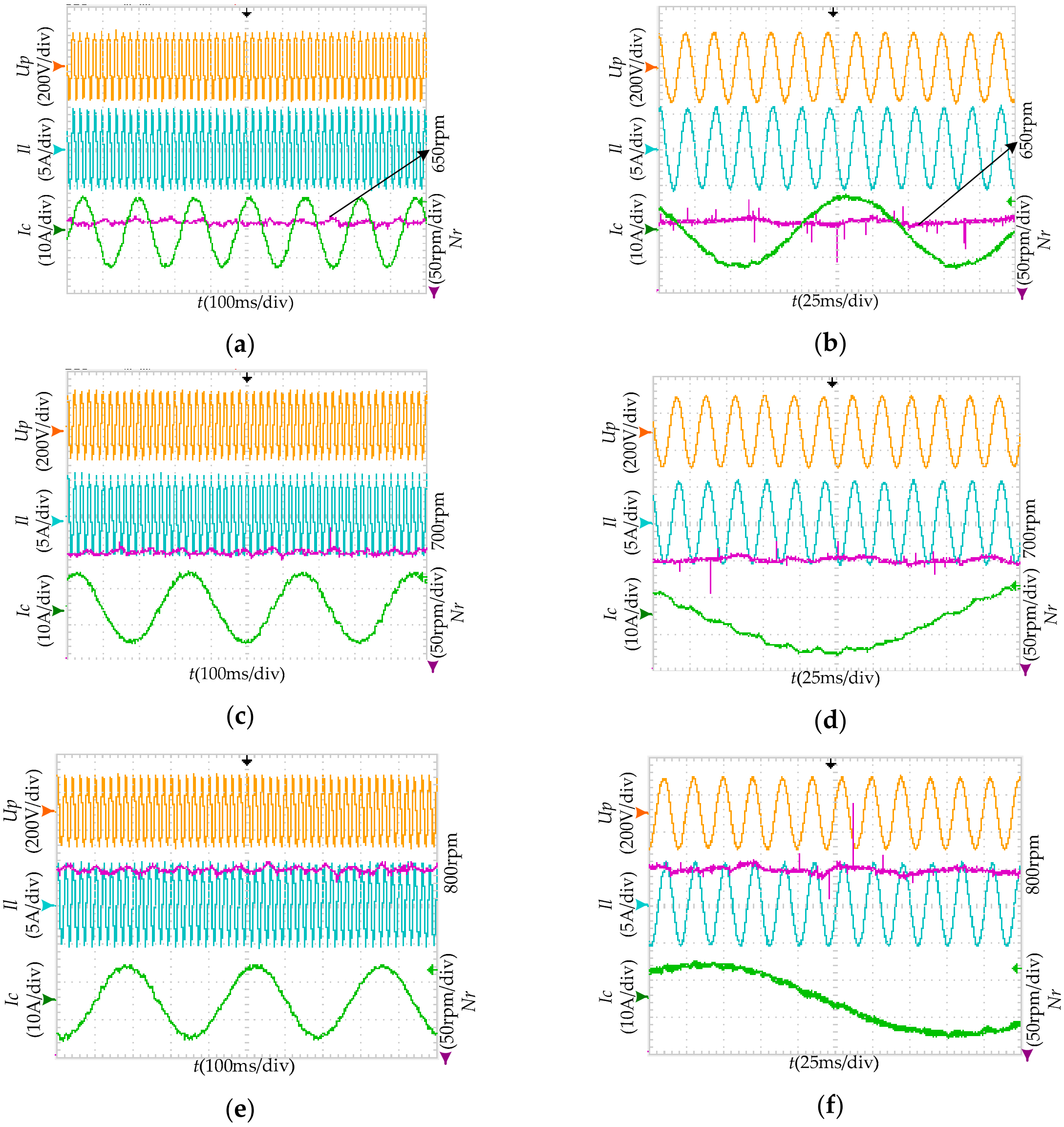

(**a**) (**b**)

(**c**) (**d**)

(**e**) (**f**)

Figure 10. *Cont.*

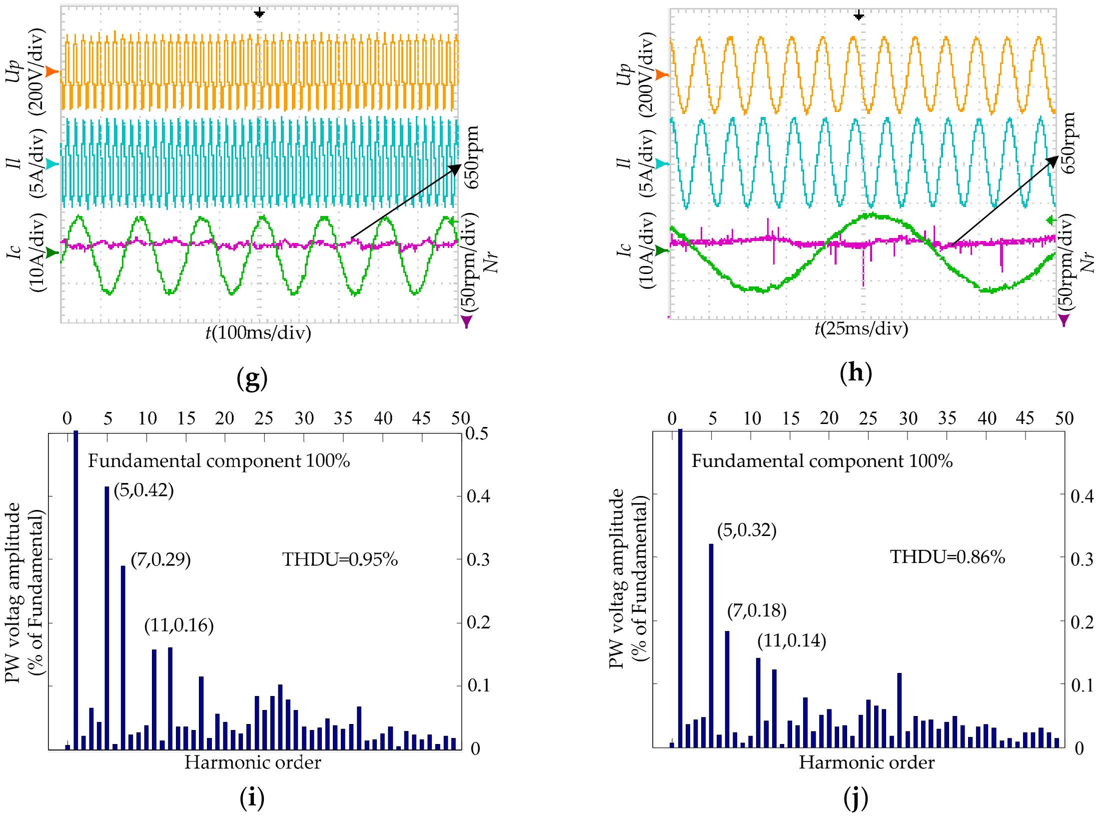

(g) (h)

(i) (j)

Figure 10. Recorded waveform of stand-alone operation BDFIG's steady state performance. (**a**) The rotor rotational velocity in sub-synchronous 700rpm; (**b**) Partial enlarged detail of **a**; (**c**) The rotor rotational velocity in sub-synchronous 650rpm; (**d**) Partial enlarged detail of **c**; (**e**) The rotor rotational velocity in super-synchronous 800rpm; (**f**) Partial enlarged detail of **e**; (**g**) The rotor rotational velocity in super-synchronous 850rpm; (**h**) Partial enlarged detail of **g**; (**i**) Harmonic spectrum FFT of PW voltage in 700rpm velocity; (**j**) Harmonic spectrum FFT of PW voltage in 800 rpm velocity.

4.3. Dynamic State Performance of Stand-alone operation BDFIG with Load Sudden Change

The dynamic response performance of the stand-alone operation BDFIG with load sudden change by R-SM-DFC approach is verified as the followings. The stand-alone operation BDFIG fed with a linear constant loads is run at sub-synchronous rotor rotational velocity of 0.933p.u.(700rpm), and an induction motor direct started supply a sudden resistance and inductance impact load, it inevitably draws sudden high inrush current for a few cycles. Figure 4a–c illustrates the recorded waveforms of PW stator terminal line voltage amplitude, load line current, CW stator phase current, PW stator voltage frequency, rotor rotational velocity and its time's partial enlarged detail, respectively. It is observed that, even if the controlling bandwidth frequency is not high, the amplitude of PW stator voltage is almost constant, the maximal instantaneous PW stator voltage amplitude drop is below 8% and the overshoot is negligibly small, and they can be recovered to the set reference values within half cycle about 10ms by regulating the CW stator voltage rapidly. The PW stator voltage frequency has a transient fluctuation approximately within the range of 0.6Hz and lasted about within 500ms. A pulsation in the rotor rotational velocity of the BDFIG inevitably occurs due to the pulsating torque when the load induction motor is started. The CW stator current are also sudden increased with the load changed, and then rapidity reach their normal value as the load current reaches steady state as shown in Figure 11c and d. For comparison purpose, the controller is also designed by traditional indirect VC methods without coupling compensation, the recorded waveforms results are presented in Figure 11g and h. Under the same load perturbations, the PW stator terminal voltage amplitude sag severely, the maximal instantaneous PW stator terminal voltage amplitude drop is approximately more than 30% and it be maintained until twenty

Peer-reviewed version available at *Energies* **2018**, *11*, 814; doi:10.3390/en11040814

cycle about 0.4sec. Thus, it can be concluded from the results that the proposed R-SM-DFC scheme prove enhanced transient performance superior to indirect VC method. The super-synchronous rotor rotational velocity of 1.067p.u.(800rpm) operation waveforms of the stand-alone operation BDFIG by R-SM-DFC scheme are also demonstrated in Figure 11d–f, the transient state performance is also similar to the case of sub-synchronous velocity operation, and the system operation is satisfactory.

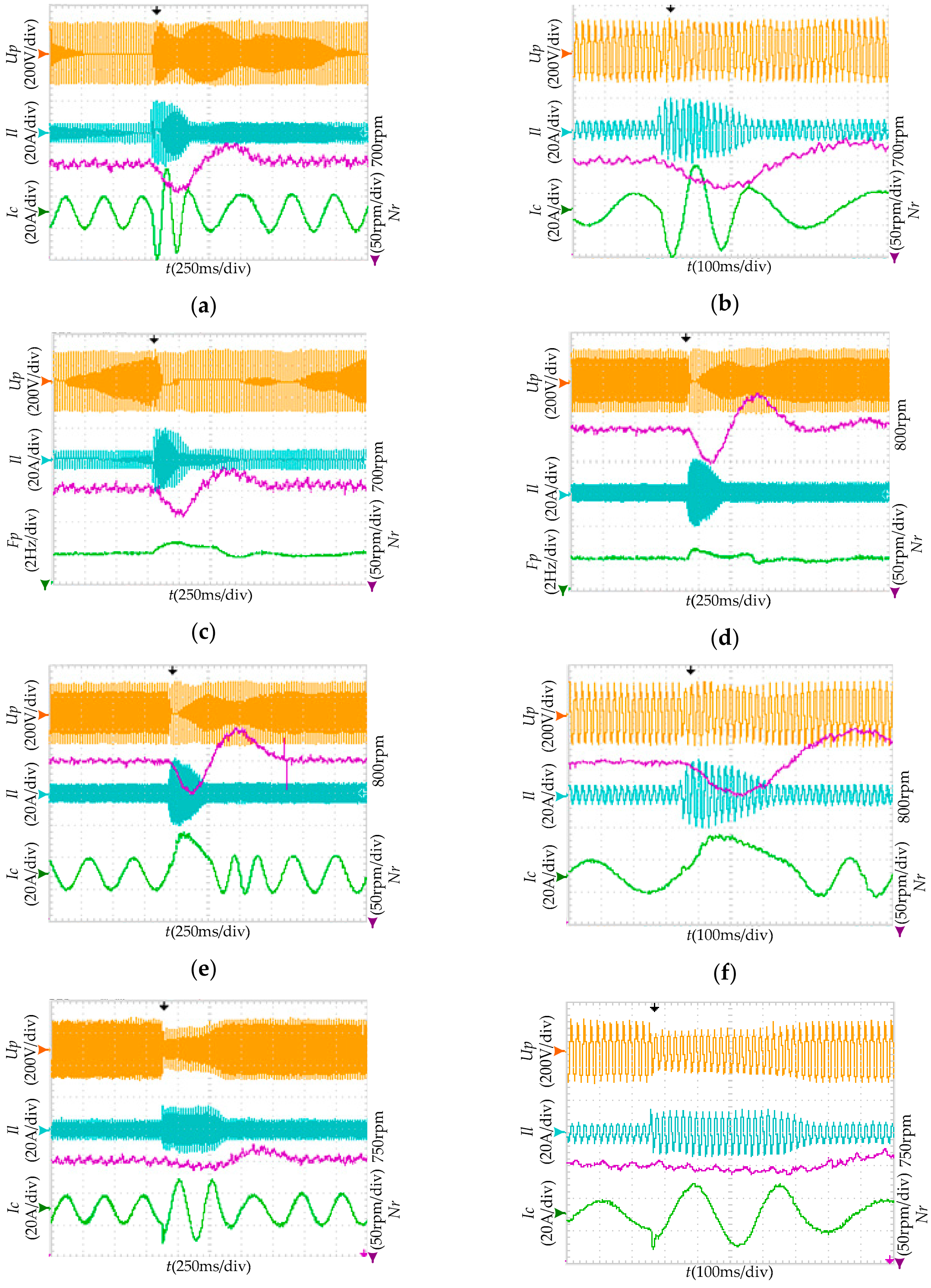

(**a**) (**b**)

(**c**) (**d**)

(**e**) (**f**)

(**g**) (**h**)

Figure 11. Recorded waveform of stand-alone operation BDFIG's dynamic state performance with load sudden change. (**a**) PW voltage amplitude etc. in sub-synchronous 700rpm velocity by

R-SM-DFC; (**b**) Partial enlarged detail of **a**; (**c**) PW voltage frequency etc. in sub-synchronous 700rpm velocity by R-SM-DFC; (**d**) PW voltage frequency etc. in super-synchronous 800rpm velocity by R-SM-DFC; (**e**) PW voltage amplitude etc. in super-synchronous 800rpm velocity by R-SM-DFC; (**f**)Partial enlarged detail of **e**; (**g**) PW voltage amplitude etc. in sub-synchronous 700rpm velocity by indirect VC; (**h**) Partial enlarged detail of **g**.

4.4. Dynamic State Performance of Stand-alone operation BDFIG with Varying Rotational Velocity

In order to investigate the accuracy and transient response of stand-alone operation at continuous variation wind speed, the dynamic performances of this proposed R-SM-DFC method are observed for the varying wind speeds as shown in Figure 12a–d. For vary in wind speed, the rotational velocity of rotor is also varying. In this case, the rotor rotational velocity will be increased from sub-synchronous velocity of 0.933p.u.(700rpm) to super-synchronous velocity of 1.067p.u.(800rpm) during 1sec with a constant linear loads. Figure 13a–b illustrates the waveforms of PW stator terminal voltage amplitude, PW stator voltage frequency, load current, CW stator phase currents, and rotor rotational velocity, respectively. From this figures, it can be observed that both the amplitude and frequency of the PW stator terminal voltage are stably maintained constant responding to reference value and independent of the rotor rotational velocity variation, the CW stator currents frequency accordingly change depending upon rotational velocity, and met the relationship of equation (1) to maintain constant frequency of the PW stator terminal voltage. Specialty, it is worthy noting that during a transition from sub-synchronous to super-synchronous velocity, the phase sequence of current flowing in the CW stator is changed, which is manifested the sign of the CW stator frequency reversed, in corresponding natural synchronous velocity, the frequency of CW stator currents is zero. Furthermore, due to the load and PW stator current being constant, the amplitude of CW stator current is same to maintain constant amplitude of the PW stator terminal voltage, in spite of change in rotor rotational velocity, nevertheless, the amplitude of CW stator voltage is must varied depending on the rotor rotational velocity to balance the varying back EMF. Moreover, in this whole process, both the PW stator and CW stator were running smoothly, and thus constant frequency, constant amplitude and sinusoidal PW stator terminal voltage was generated to the load with low harmonic distortion. Similar accuracy and response performances has been observed in Figure 12c–d when the rotor rotational velocity will be decreased from super-synchronous velocity of 1.067p.u.(800rpm) to sub-synchronous velocity of 0.933p.u.(700 rpm), during 1sec with a constant linear load. Hence, the BDFIG is controlled properly by R-SM-DFC scheme when the rotor rotational velocity changes quickly.

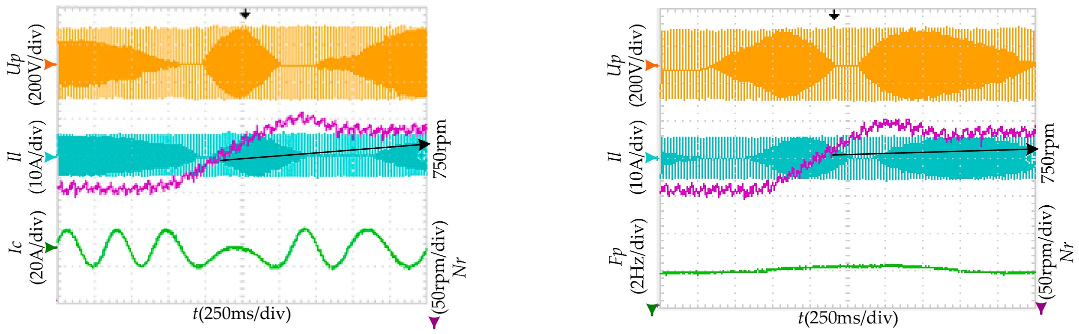

(**a**) (**b**)

Figure 12. *Cont.*

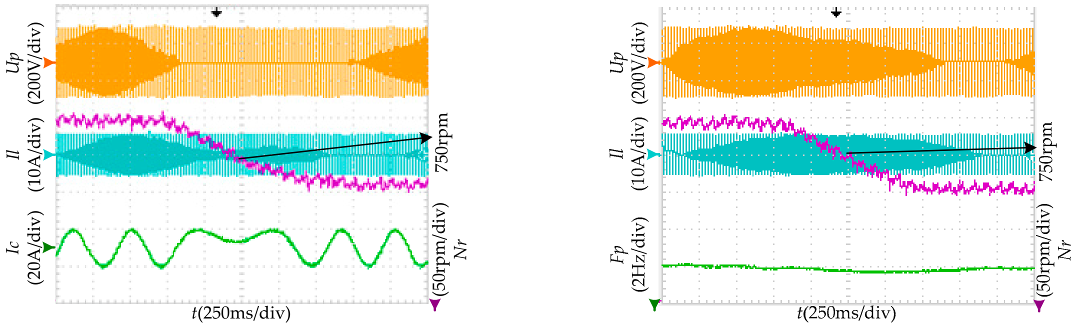

(**c**) (**d**)

Figure 12. Recorded waveform of stand-alone operation BDFIG's dynamic state performance with varying rotor rotational velocity. (**a**) PW voltage amplitude etc. with the rotor rotational velocity from sub-synchronous to super-synchronous; (**b**) PW voltage frequency etc. with the rotor rotational velocity from sub-synchronous to super-synchronous; (**c**) PW voltage amplitude etc. with the rotor rotational velocity from super-synchronous to sub-synchronous; (**d**) PW voltage frequency etc. with the rotor rotational velocity from super-synchronous to sub-synchronous.

5. Conclusions

This paper has addressed the stand-alone operation BDFIG complete control solution for VSCF WECS. The pretty well contribution of the proposed control method is to combine the DC strategy, SMC approach, and SVM modulation technique, so as to directly regulate PW stator flux by calculating and adjusting the CW stator voltage. Owing to no extra CW stator current control loops involved, therefore simplifying the system configuration design and enhancing the transient performance. Thanks to be implemented in the PW stator stationary reference frame, no synchronous rotating coordinate transformations and angular information of grid voltage or PW stator flux are required. The nonlinear ROGI based resonant sliding surface is introduced to eliminate the AC tracking error. Constant converter switching frequency was achieved by employing SVM technique, which reduce the harmonic spectra. The steady and dynamic state performance is validated via experiments of a prototype, as a result, enhanced transient performance similar to the DC scheme is obtained and steady-state PW stator terminal voltage harmonic spectra are kept at the same level as the VC strategy. The future work is progress to develop the control scheme for operation without rotor rotational velocity sensor, and supply unbalance or nonlinear isolated load.

Acknowledgments: The authors are grateful to the Key Projects in the National Science & Technology Pillar Program of China (2012BAG03B01) during the Twelfth Five-year Plan Period, and National Natural Science Foundation of China (51377064) for supporting this work.

Author Contributions: Kai Ji handled the project as the first author. Kai Ji contributed to the conception of the study and the control algorithm, then, conceived, designed and performed the experiments, and analyzed the data. Shenghua Huang advised the method of the proposed algorithm and helped to perform the analysis with constructive discussions. All authors provided substantive comments.

Conflicts of Interest: The authors declare no conflict of interest.

References

1. Polinder, H.; Ferreira, J.A.; Jensen, B.B.; Abrahamsen, A.B.; Atallah, K.; McMahon, R.A. Trends in wind turbine generator systems. *IEEE Jour. Emer. Sel. Top. Power Electron.* **2013**, *1*, 174-185.
2. Strous, T.D.; Polinder, H.; Ferreira, J.A. Brushless doubly-fed induction machines for wind turbines: developments and research challenges. *IET Elect. Power Appl.* **2017**, *11*, 991-1000.
3. Tohidi, S.; Tavner, P.; McMahon, R.A. Low voltage ride-through of DFIG and brushless DFIG: similarities and differences. *Elect. Power Syst. Res.* **2014**, *110*, 64-72.

Peer-reviewed version available at *Energies* **2018**, *11*, 814; doi:10.3390/en11040814

4. Poza, J.; Oyarbide, E.; Sarasola, I.; Rodriguez, M.A. Vector control design and experimental evaluation for the brushless doubly fed machine. *IET Elect. Power Appl.* **2009**, *3*, 247-256.
5. Shao, S.Y.; Abdi, E.; Barati, F.; McMahon, R.A. Stator-flux-oriented vector control for brushless doubly-fed induction generator. *IEEE Trans. Ind. Electron.* **2009**, *56*, 4220-4228.
6. Shao, S.Y.; Long, T.; Abdi, E.; McMahon, R.A. Dynamic control of the brushless doubly fed induction generator under unbalanced operation. *IEEE Trans. Ind. Electron.* **2013**, *60*, 2465-2476.
7. Chen, J.F.; Zhang, W.; Chen, B.J.; Ma, Y.L. Improved vector control of brushless doubly fed induction generator under unbalanced grid conditions for offshore wind power generation. *IEEE Trans. Energy Conv.* **2016**, 31, 293-302.
8. Shipurkar, U.; Strous, TM.; Polinder, H.; Ferreira, J.A.; Veltman, A. Achieving sensorless control for the brushless doubly fed induction machine. *IEEE Trans. Energy Conv.* **2017**, *32*, 1611-1619.
9. Chaal, H.; Jovanovic, M. Toward a generic torque and reactive power controller for doubly fed machines. *IEEE Trans. Power Electron.* **2012**, *27*, 113-121.
10. Sarasola, I.; Poza, J.; Rodriguez, M.A.; Abad, G. Direct torque control design and experimental evaluation for the brushless doubly fed machine. *Energy Conv. Manage.* **2011**, *52*, 1226-1234.
11. Hu, J.F.; Zhu, J.G.; Dorrell, D.G. A new control method of cascaded brushless doubly fed induction generators using direct power control. *IEEE Trans. Energy Conv.* **2014**, *29*, 771-779.
12. Xia, C.L.; Hou, X.X. Study on the static load capacity and synthetic vector direct torque control of brushless doubly fed machines. *Energies* **2016**, *9*, 966-988.
13. Sarasola, I.; Poza, J.; Rodriguez, M.A.; Abad, G. Predictive direct torque control for brushless doubly fed machine with reduced torque ripple at constant switching frequency. *IEEE Int. Sym. Ind. Electro.*, Vigo, Spain, 4-7 June **2007**.
14. Ji, K.; Huang, S.H.; Zeng, C.; Gao, Y. Direct voltage control using space vector modulation for stand-alone brushless doubly fed induction generator. *Trans. China Electro. Society* **2015**, *30*, 186-196.
15. Zhao, R.L.; Zhang, A.L.; Ma, Y.; W.X.; Yan, J.; Ma, Z.Z. The dynamic control of reactive power for the brushless doubly fed induction machine with indirect stator-quantities control scheme. *IEEE Trans. Power Electron.* **2015**, *30*, 5046-5057.
16. Liu, Y.; Ai, W.; Chen, B.; Chen, K.; Luo, G. Control design and experimental verification of the brushless doubly-fed machine for stand-alone power generation applications. *IET Elect. Power Appl.* **2016**, *10*, 25-35.
17. Sun, L.; Chen, Y.; Su, J.Y.; Zhang, D.B.; Peng, L.; Kang, Y. Decoupling network design for inner current loops of stand-alone brushless doubly fed induction generation power system. *IEEE Trans. Power Electron.* **2018**, *33*, 957-963.
18. Cheng, M.; Jiang, Y.L.; Han, P.; Wang, Q.S. Unbalanced and low-order harmonic voltage mitigation of stand-alone dual-stator brushless doubly fed induction wind generator. *IEEE Trans. Ind. Electron. accepted.*
19. Wei, X.C.; Cheng, M.; Wang, W.; Han, P.; Luo, R.S. Direct voltage control of dual-stator brushless doubly fed induction generator for stand-alone wind energy conversion systems. *IEEE Trans. Mag.* **2016**, *52*, *Article Sequence Number:* 8203804.
20. Wang, X.W.; Lin, H.; Wang, Z. Transient control of the reactive current for the line-side converter of the brushless doubly-fed induction generator in stand-alone operation. *IEEE Trans. Power Electron.***2017**, *32*, 8193-8203.
21. Barambones, O.; Cortajarena, J.A.; Alkorta,P.; Gonzalez de Durana, J.M. A real-time sliding mode control for a wind energy system based on a doubly fed induction generator. *Energies* **2014**, *7*, 6412-6433.
22. Susperregui, A.; Tapia, G; Zubia, I.; Ostolaza, J.X. Sliding-mode control of doubly-fed generator for optimum power curve tracking. *Electron. Let.* **2010**, *46*, 126-127.
23. Hu, J.B.; Shang, L.; He, Y.K.; Zhu, Z.Q. Direct active and reactive power regulation of grid-connected DC/AC converters using sliding mode control approach. *IEEE Trans. Power Electron.* **2011**, *26*, 210-222.
24. Chen, S.Z.; Cheung, N.C.; Wong, K.C.; Wu, J. Integral variable structure direct torque control of doubly fed induction generator. *IET Renew. Power Gene.* **2011**, *5*, 18-25.
25. Martinez, M.I.; Susperregui, A.; Tapia, G. Second-order sliding-mode-based global control scheme for wind turbine-driven DFIGs subject to unbalanced and distorted grid voltage. *IET Elect. Power Appl.* **2017**, *11*, 1013-1022.
26. Liu, X.J.; Han, Y.Z.; Wang, C.C. Second-order sliding mode control for power optimisation of DFIG-based variable speed wind turbine. *IET Renew. Power Gene.* **2017**, *11*, 408-418.

Peer-reviewed version available at *Energies* **2018**, *11*, 814; doi:10.3390/en11040814

27. Djoudi, A.; Bacha, S.; Chekireb, H.; Iman-Eini, H.; Boudinet, C. Adaptive sensorless SM-DPC of DFIG-based WECS under disturbed grid: study and experimental results. *IEEE Trans. Sustain. Energy. accepted*.
28. Ullah, N.; Ali, M.A.; Ibeas, A.; Herrera, J. Adaptive fractional order terminal sliding mode control of a doubly fed induction generator-based wind energy system. *IEEE Access.* **2017**, *5*, 21368-21381.
29. Xiong, L.Y.; Wang, J.; Mi, X.; Khan, M.W. Fractional order sliding mode based direct power control of grid-connected DFIG. *IEEE Trans. power Sys. accepted*.
30. Esfandiari, G.; Author 2, C.D.; Ebrahimi, M.; Tabesh, A.; Esmaeilzadeh, M. Dynamic modeling and analysis of cascaded DFIMs in an arbitrary reference frame. *IEEE Trans. Energy Conv.* **2015**, *30*, 999-1007.
31. Jorge, S.G.; Busada, C.A.; Solsona, J. Low computational burden grid voltage sensorless current controller. *IET Power Electron.* **2013**, *6*, 1592-1599.